Chinese Chemical Letters 36 (2025) 110663

Contents lists available at ScienceDirect

Chinese Chemical Letters

journal homepage: www.elsevier.com/locate/cclet

Hierarchical zeolites stabilized cobalt(II) as propane dehydrogenation catalyst: Enhanced activity and coke tolerance *via* alkaline post-treatment

Kun Yang[a], Anhui Li[c], Peng Zhang[b], Guilin Liu[a], Liusai Huang[a], Yumeng Fo[a], Luyuan Yang[a], Xiangyang Ji[a], Jian Liu[a], Weiyu Song[a,*]

[a] *State Key Laboratory of Heavy Oil Processing, China University of Petroleum, Beijing 102249, China*
[b] *Petrochemical Research Institute, PetroChina Company Limited, Beijing 102206, China*
[c] *SINOPEC Safety Engineering Institute, Qingdao 266071, China*

ARTICLE INFO

Article history:
Received 23 September 2024
Revised 18 November 2024
Accepted 21 November 2024
Available online 22 November 2024

Keywords:
Propane dehydrogenation
Hierarchical zeolites
Different alkaline treatment
Cobalt catalyst
Coke tolerance

ABSTRACT

Transition metal cobalt exhibits strong activation capabilities for alkanes, however, the instability of Co sites leads to sintering and coke deposition, resulting in rapid deactivation. Hierarchical zeolites, with their diverse pore structures and high surface areas, are used to effectively anchor metals and enhance coke tolerance. Herein, a post-treatment method using an alkaline solution was employed to synthesize meso–microporous zeolite supports, which were subsequently loaded with Co species for propane dehydrogenation catalyst. The results indicate that the application of NaOH, an inorganic base, produces supports with a larger mesopore volume and more abundant hydroxyl nests compared to TPAOH, an organic base. UV–vis, Raman, and XPS analyses reveal that Co in the 0.5Co/SN-1–0.05 catalyst is mainly in the form of tetrahedral Co^{2+}, which effectively activates C–H bonds. In contrast, the 0.5Co/S-1 catalyst contains mainly Co_3O_4 species. Co^{2+} supported on hierarchical zeolites shows better propane conversion (58.6%) and propylene selectivity (>96%) compared to pure silica zeolites. Coke characterization indicates that hierarchical zeolites accumulate more coke, but it is mostly in the form of easily removable disordered carbon. The mesopores in the microporous zeolite support help disperse the active Co metal and facilitate coke removal during dehydrogenation, effectively preventing deactivation from sintering and coke coverage.

Propylene is a key chemical feedstock with significant market demand, serving as a precursor for important chemicals such as polypropylene, propylene oxide, acrylonitrile, and other derivatives. The propane dehydrogenation (PDH) process for propylene production has garnered considerable attention and research due to its high propylene selectivity and favorable product purity [1,2]. Industrially, PDH catalysts are predominantly Pt-based or CrO_x-based. However, Pt is costly, while CrO_x catalysts suffer from severe coke formation and Cr species aggregation at high temperatures, leading to rapid deactivation and irreversible environmental and health hazards from Cr^{6+} [3–5]. Transition metals, with their abundant reserves, strong alkane activation capabilities, and environmental benignity, have recently been extensively explored for PDH reactions. Among them, Co-based catalysts have emerged as a research focus due to their effective C–H bond activation and high olefin selectivity [6–9].

However, Co-based catalysts still face the issue of low stability, which is far from meeting the demand. The main reasons are as follows: First, PDH is a high-temperature reaction, typically carried out at temperatures exceeding 520 °C. At these elevated temperatures, the active metal the active metal components tend to sinter, leading to catalyst deactivation [10]. Therefore, it is essential to improve the anchoring of the active components, enhance the diffusion rate, and increase the support's resistance to coke formation [11].

Microporous zeolites serve as ideal supports for metal species because of their ordered pore structures and high surface areas. However, traditional microporous zeolites generally suffer from narrow intrinsic pore channels and limited compositional diversity, which restrict their applications. Currently, considerable research efforts are focused on introducing mesopores into microporous zeolite crystals to create hierarchical porous zeolites with at least

---

* Corresponding author.
E-mail address: songwy@cup.edu.cn (W. Song).

https://doi.org/10.1016/j.cclet.2024.110663

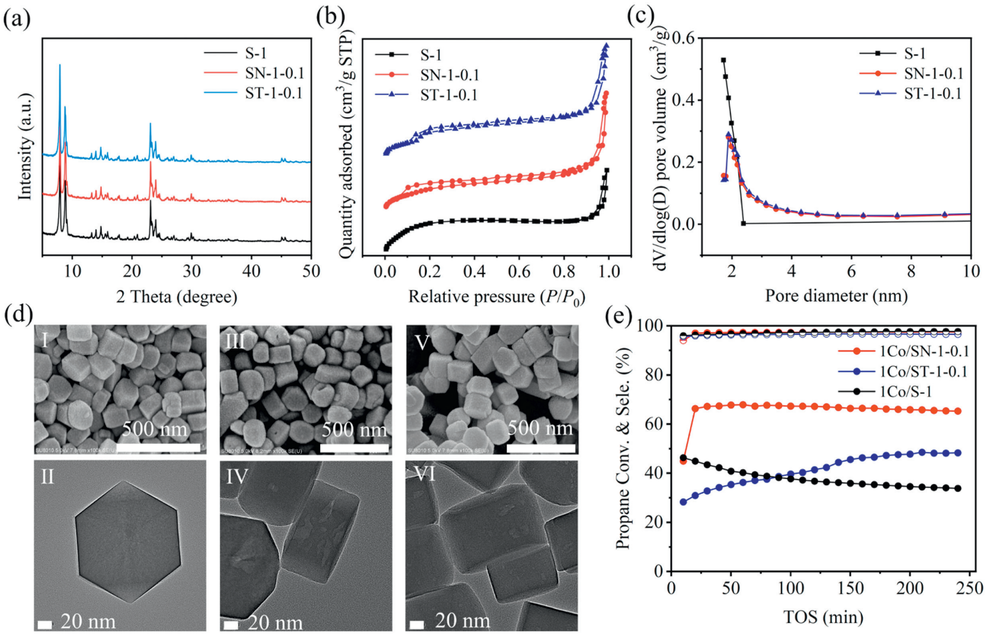

Fig. 1. (a) XRD patterns of S-1 zeolites treated with different alkaline sources. (b) N_2 adsorption-desorption isotherms and (c) pore size distributions from BJH adsorption for zeolites. (d) SEM and TEM images: I-II, S-1; III-IV, SN-1–0.1; V-VI, ST-1–0.1. (e) Propane conversion and propylene selectivity (reaction conditions: 580 °C, 0.2 g catalyst, 5 vol% propane balanced with N_2, 10 mL/min).

two types of pores (intrinsic micropores and mesopores). Compared to traditional zeolites, hierarchical zeolites, with their mesopores, not only facilitate the mass transfer of substrates and products, thereby reducing coke formation, but also enhance the support's coke resistance, thereby significantly improving catalyst activity and stability [12]. There are mainly two methods for synthesizing hierarchical zeolites: a bottom-up direct synthesis approach and a top-down post-treatment approach. Compared to direct synthesis, the post-treatment method is simpler and more controllable [13,14].

Herein, various types and concentrations of alkaline solutions were used to treat silicate-1 (S-1) zeolite, resulting in mesopores of varying sizes. Subsequently, a series of catalysts were prepared by loading Co species onto the treated supports using an incipient wetness impregnation method. Among these, the catalyst derived from Co-loaded S-1 treated with a 0.05 mol/L NaOH solution (0.5Co/SN-1–0.05) exhibited the best performance, exhibiting nearly 6 times the catalytic activity of the untreated Co/S-1 catalyst. The increased mesopore volume generated after treatment not only facilitated the dispersion of metal species but also significantly enhanced the catalyst's coke resistance.

The XRD patterns of S-1 after non-alkali source treatment are shown in Fig. 1a. The results indicate that both the parent zeolite and the zeolites treated with two different alkaline solutions exhibit characteristic peaks corresponding to the MFI topology at $2\theta = 7.9°$, 8.7°, and 22°–25° [15]. The diffraction peak intensities of all samples are essentially similar, suggesting that the two alkaline treatments do not significantly affect the crystal structure of S-1 zeolite. The N_2 physical adsorption desorption experiment (Figs. 1b and c) reveal that the S-1 zeolite exhibits a Type I isotherm, indicative of a conventional microporous structure [16]. In contrast, SN-1–0.1 and ST-1–0.1 samples show varying degrees of an H3-type hysteresis loop, with the loop being more obvious for the NaOH-treated SN-1–0.1 sample [17]. The structural data and pore size distribution (as shown in Table S1 in Supporting information) indicate that the mesopore volume of both samples increases after alkaline treatment, while the specific surface area and micropore volume decrease. This reduction is attributed to the partial destruction of the micropore structure during the alkaline removal of framework silica. Moreover, the mesopore volume of NaOH-treated SN-1–0.1 is obviously larger than that of TPAOH-treated ST-1–0.1, and the micropore volume is basically the same, which is consistent with the adsorption-desorption curve results, indicating that SN-1–0.1 contains a higher quantity of mesopores. This observation is further supported by the TEM images in Fig. 1d, which show a greater and more obvious presence of mesopores in SN-1–0.1 compared to ST-1–0.1. Subsequently, the three supports were impregnated with the same amount of cobalt, and the resulting samples were tested for propane dehydrogenation activity (Fig. 1e). The results indicate that the initial activity of the 1Co/S-1 sample, which was not treated, is intermediate between the 1Co/SN-1–0.1 and 1Co/ST-1–0.1 samples, which were treated with NaOH and TPAOH solutions, respectively. Although the initial activity of the 1Co/ST-1–0.1 sample is lower than that of 1Co/S-1, it exhibits better stability and has a certain induction period. This induction period may be attributed to the dynamic evolution of the active cobalt sites (Fig. S1 in Supporting information). Conversely, the 1Co/SN-1–0.1 sample demonstrates both higher initial activity and stability compared to 1Co/S-1. This indicates that alkaline treatment significantly enhances the stability of the samples and that cobalt supported on NaOH-treated support shows superior activity. The improvement in stability is attributed to the enhanced capacity of the mesopores formed by alkaline treatment to accommodate carbon deposition, thereby effectively mitigating deactivation [18]. The observed differences in initial activity between the different alkaline treatments may be due to the role of TPAOH solution. As a template agent for S-1 zeolite, TPAOH not only dissolves the parent zeolite but also induces the re-growth of crystals on the surface of the parent zeolite, resulting in fewer surface defects and less cobalt species distributed within the mesopores, which leads to lower activity [19,20].

Subsequently, the effects of NaOH solution with different concentrations on the S-1 zeolite were studied, as shown in Fig. 2a. All samples exhibit characteristic diffraction peaks of the MFI framework structure, indicating that increasing the concentration of the alkali solution does not lead to complete collapse of the zeolite

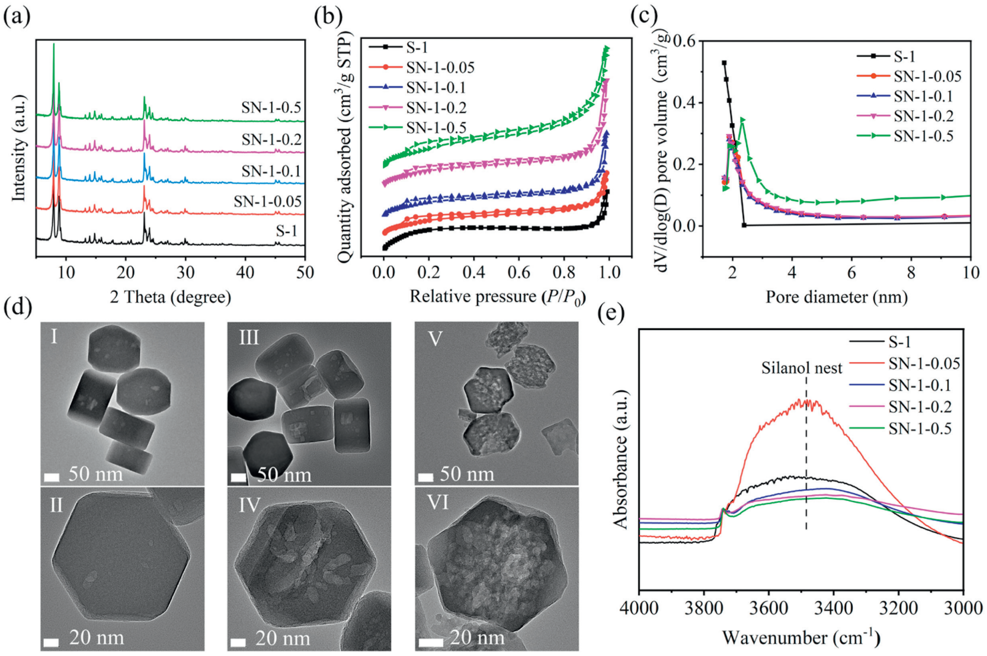

Fig. 2. (a) XRD patterns of S-1 zeolites treated with different alkaline concentrations. (b) N_2 adsorption-desorption isotherms and (c) pore size distributions from BJH adsorption for zeolites. (d) TEM images: I-II, SN-1–0.05; III, SN-1–0.1; IV, SN-1–0.2; V-VI, SN-1–0.5. (e) OH-FTIR spectra.

framework. However, it is noticed that with increasing alkali concentration, the intensity of the diffraction peaks decreases significantly. According to the relative crystallinity (Table S2 in Supporting information), this suggests that higher alkali concentrations result in greater dissolution of the zeolite framework silicon, more mesopore formation, and larger mesopore sizes (Figs. 2b and c, and Table S3 in Supporting information) [21,22]. Similarly, TEM images also reveal the presence of pronounced mesopore structures within the zeolite after alkali treatment (Fig. 2d). As the concentration of the alkali solution increases, the number of mesopores within the zeolite increases; however, excessive alkali concentration leads to severe structural damage, resulting in fragmentation and collapse (Fig. S2 in Supporting information). To further explore the effect of different alkali concentrations on the number of hydroxyl sites in the zeolite, the OH-FTIR spectrum is shown in Fig. 2e. The peak at 3740 cm^{-1} attributed to the stretching vibration of the terminal hydroxyl groups in the zeolite, and the peaks from 3600 cm^{-1} to 3300 cm^{-1} are attributed to the hydroxyl groups in the silanol nests, *i.e.*, the vibration peaks of the hydroxyl nests [23]. The results show that as the concentration of the alkali treatment solution increases, the number of hydroxyl nests in the S-1 zeolite follows a volcano-type trend, initially increasing and then decreasing. The maximum content of hydroxyl nests is observed in the zeolite treated with a 0.05 mol/L alkali solution.

Characterization of hydroxyl groups revealed that the support treated with 0.05 mol/L NaOH solution has a higher content of hydroxyl nests, which are often associated with the presence of active sites. Therefore, catalysts 0.5Co/SN-1–0.05 and 0.5Co/S-1 were prepared using the NaOH-treated SN-1–0.05 and untreated S-1 zeolites as supports, respectively, to investigate the effects of hydroxyl nests and mesopores generated by alkali treatment. The XRD patterns of both catalysts show no diffraction peaks corresponding to Co species, indicating that Co species are uniformly distributed on the support (Fig. 3a) [24]. After Co loading, both catalysts exhibit a decrease in micropore volume, suggesting that metal sites occupy a portion of the micropores (Figs. 3b and c). SEM mapping results (Fig. 3d) show that the Co species in both catalysts are uniformly distributed as small particles, highly dispersed on the hierarchical pore supports, with no evidence of larger particles or agglomeration.

Subsequently, the performance of the catalysts in propane dehydrogenation reactions was evaluated. The cobalt contents in the 0.5Co/SN-1–0.05 and 0.5Co/S-1 samples are 0.48 wt% and 0.44 wt%, respectively, as determined by ICP-OES. There was a significant difference in catalytic activity between the two samples (Fig. 4a). The 0.5Co/SN-1–0.05 sample exhibited an initial propane conversion rate of 58.6% with a propylene selectivity of 97.5%. In contrast, the 0.5Co/S-1 sample showed a much lower conversion rate of only 12.1%, with propylene selectivity also lower than that of 0.5Co/SN-1–0.05. The stability of the 0.5Co/SN-1–0.05 catalyst was tested over a 12-h period for propane dehydrogenation (Fig. S3 in Supporting information). The 0.5Co/SN-1–0.05 catalyst reached a maximum conversion rate of 59.2% after 100 min of reaction and maintained a conversion rate of 50.2% after 12 h, with a deactivation rate constant (k_d) of 0.033 h^{-1}, indicating very slow deactivation and good stability for propane dehydrogenation. Kinetic experiments were then conducted to investigate the intrinsic activity of the two samples in the PDH reaction. Fig. 4b shows the Arrhenius plots for each catalyst. The apparent activation energy (E_a) or the 0.5Co/S-1 sample was 137.67 kJ/mol, while the apparent activation energy for the 0.5Co/SN-1–0.05 sample was only 70.08 kJ/mol, approximately half of the former, indicating a lower dehydrogenation barrier for 0.5Co/SN-1–0.05. Similarly, at 550 °C, the turnover frequencies (TOF) for the 0.5Co/S-1 and 0.5Co/SN-1–0.05 samples were 12.04 h^{-1} and 42.58 h^{-1}, respectively, with the TOF for 0.5Co/SN-1–0.05 being 3.5 times higher than that for 0.5Co/S-1 (Fig. 4c). These results demonstrate that the intrinsic activity of 0.5Co/SN-1–0.05 is significantly higher than that of 0.5Co/S-1, indicating a fundamental difference in the state of active sites. Additionally, the regeneration performance of the 0.5Co/SN-1–0.05 sample was tested (Fig. 4d). After three regeneration cycles, the initial conversion rate remained at 60.5%, with propylene selectivity consistently around 97%, demonstrating excellent regeneration stability of the 0.5Co/SN-1–0.05 catalyst.

Based on the above results, it is evident that the active sites of the two samples should have distinct characteristics, thus fur-

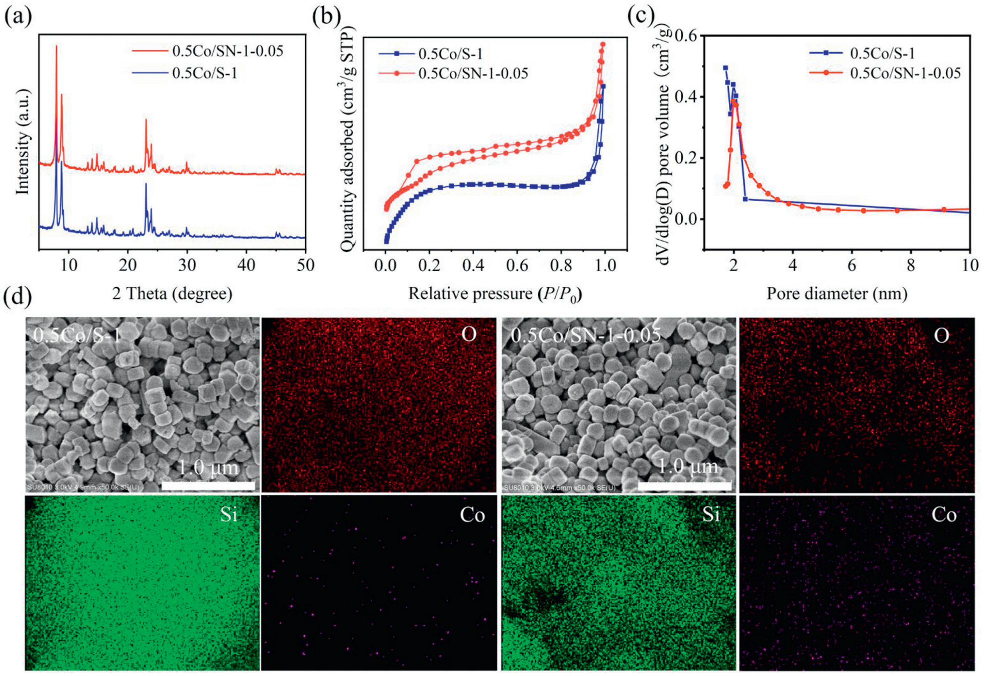

Fig. 3. (a) XRD patterns of 0.5Co/S-1 and 0.5Co/SN-1–0.05. (b) N_2 adsorption-desorption isotherms and (c) pore size distributions from BJH adsorption for zeolites. (d) SEM and EDS images.

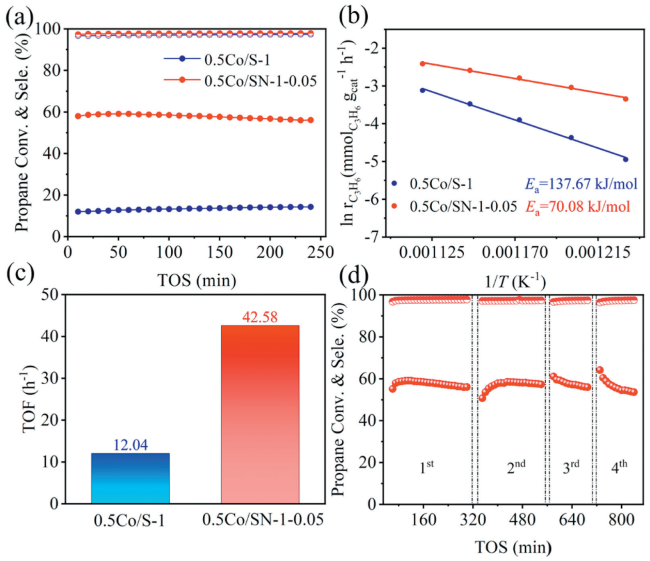

Fig. 4. (a) Propane conversion and propylene selectivity for 0.5Co/S-1 and 0.5Co/SN-1–0.05 (reaction conditions: 580 °C, 0.2 g catalyst, 5 vol% propane balanced with N_2, 10 mL/min). (b) Arrhenius curves and apparent activation energies of 0.5Co/S-1 and 0.5Co/SN-1–0.05. (c) TOF comparison of sample 0.5Co/S-1 and 0.5Co/SN-1–0.05 (reaction conditions: 550 °C, 0.5Co/SN-1–0.05: 0.1 g, 5 vol% propane balanced with N_2, 45 mL/min; 0.5Co/SN-1–0.05: 0.1 g, 5 vol% propane balanced with N_2, 25 mL/min). (d) Regeneration test for 0.5Co/SN-1–0.05 catalyst.

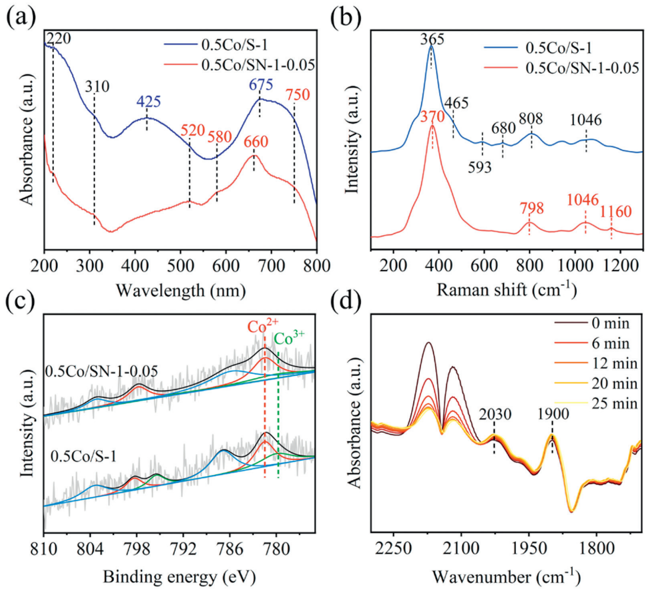

Fig. 5. (a) UV–vis spectra of 0.5Co/S-1 and 0.5Co/SN-1–0.05 catalysts. (b) Raman spectra of 0.5Co/S-1 and 0.5Co/SN-1–0.05 catalysts. (c) XPS profiles of 0.5Co/S-1 and 0.5Co/SN-1–0.05 catalysts. (d) *In-situ* DRIFT spectra with CO flows.

ther research was conducted into the state of the Co species in the sample active sites. UV–vis spectroscopy was used to probe the oxidation states and coordination geometry of the Co species in different forms. As shown in Fig. 5a, both samples exhibit two absorption peaks at 220 nm and 310 nm, corresponding to the MFI framework structure of the zeolite. The 0.5Co/SN-1–0.05 catalyst shows characteristic peaks around 520 nm, 580 nm, and 660 nm, attributed to the d-d transitions of tetrahedrally coordinated Co(II) ($^4A_2(F) \rightarrow {}^4T_1(P)$), indicating the presence of Co^{2+} in a tetrahedral coordination within the zeolite framework. In contrast, the 0.5Co/S-1 sample shows a weak peak at 675 nm, suggesting the presence of only a partial amount of Co^{2+} on the surface of 0.5Co/S-1. Additionally, broad absorption bands at 425 nm and 750 nm are observed, associated with the $O^{2-} \rightarrow Co^{2+}$ and $O^{2-} \rightarrow Co^{3+}$ charge-transfer transitions in Co_3O_4 [25–27]. Therefore, the primary form of Co species in 0.5Co/SN-1–0.05 is tetrahedrally coordinated Co^{2+}, while in 0.5Co/S-1, Co species mainly exist in the form of Co_3O_4. Similarly, Raman spectroscopy results (Fig. 5b) show comparable findings. Two distinct Raman bands at approximately 370 cm^{-1} and 800 cm^{-1} correspond to the MFI

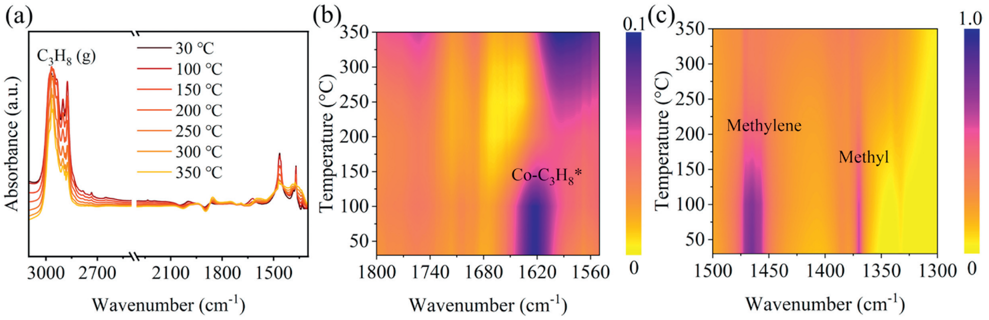

Fig. 6. (a) *In situ* C_3H_8-DRIFT spectra. (b, c) Color mapping spectra.

topology of the zeolite. New Raman bands at 465 cm^{-1}, 593 cm^{-1}, and 680 cm^{-1} in the 0.5Co/S-1 catalyst are attributed to Co_3O_4 species. The Raman band at 1046 cm^{-1} corresponds to the asymmetric stretching vibration of $Co^{\delta+}$-O-Si in the framework, while the Raman band at 1160 cm^{-1} in the 0.5Co/SN-1–0.05 catalyst indicates successful incorporation of Co atoms into the zeolite framework [28,29]. XPS analysis of Co 2p (Fig. 5c) reveals two broad and asymmetric main peaks in both samples at 775–790 eV and 790–810 eV, corresponding to Co $2p_{3/2}$ and Co $2p_{1/2}$, respectively [30]. The 0.5 Co/S-1 catalyst shows two spin-orbit double peaks for Co^{2+} and Co^{3+} and a broad satellite peak, with 781.5 eV assigned to Co^{2+}, 780.0 eV to Co^{3+}, and a Co^{2+}/Co^{3+} ratio of 1.51. The 0.5Co/SN-1–0.05 catalyst also shows characteristic peaks corresponding to Co^{2+} and Co^{3+}, with a Co^{2+}/Co^{3+} ratio of 3.39. This indicates that the Co species in the 0.5 Co/SN-1–0.05 catalyst mainly exist in the form of tetrahedral Co^{2+} anchored to the zeolite framework, while the Co species in the 0.5 Co/S-1 catalyst are mostly in the form of Co_3O_4 aggregates [31,32]. Furthermore, *in-situ* FTIR spectroscopy (Fig. 5d) was used to analyze the Co species under CO adsorption conditions. The double peaks in the range of 2100 cm^{-1} to 2300 cm^{-1} represent the characteristic peaks of free CO gas, while the peak at 1900 cm^{-1} is associated with the zeolite. The peak at 2030 cm^{-1} is attributed to CO adsorption on the linear coordination of Co^{2+} species in the zeolite framework [32]. These results indicate that the Co species in 0.5Co/SN-1–0.05 are predominantly in the form of Co^{2+} anchored to the zeolite framework, while the Co species in 0.5Co/S-1 are mainly in the form of aggregated Co_3O_4. The differences in the active sites account for the distinctly different performances observed in the PDH reaction. The reason for this difference in active sites may be due to the fact that $[Co(H_2O)_6]^{2+}$ generated from $Co(NO_3)_2$ dissolution in water has difficulty entering the untreated S-1 zeolite channels. In contrast, alkali treatment generates mesopores that allow $[Co(H_2O)_6]^{2+}$ to easily penetrate the zeolite and become anchored by hydroxyl nests[32]. Consequently, only a minimal amount of Co species enters the S-1 zeolite, with most remaining on the surface, resulting in Co_3O_4 dominance in 0.5Co/S-1. Conversely, the abundant mesopores and hydroxyl nests in SN-1–0.05 facilitate the good dispersion and anchoring of Co species within the zeolite, leading to a predominance of unitary Co^{2+} in 0.5Co/SN-1–0.05.

In situ infrared spectroscopy of propane (Fig. 6a) was used to investigate the dehydrogenation mechanism of the active sites. At the initial temperature of 50 °C, an absorption band at 2967 cm^{-1}, corresponding to gas-phase propane, was immediately detected. As the temperature increased, the intensity of the bands at 1370 cm^{-1} and 1456 cm^{-1} gradually decreased. These bands are attributed to the C–H vibrations of propane methyl groups and methylene groups adsorbed on cobalt, respectively. The weakening of the C–H vibration peaks indicates the transformation of propane. The contour map provides a clearer comparison of the changes in the characteristic peaks with temperature for the two samples (Figs. 6b and c). The peak associated with methyl groups begins to weaken at 150 °C and nearly disappears at 250 °C, while the methylene peak remains significantly visible at 300 °C. This suggests that for the 0.5Co/SN-1–0.05 sample, the propane dehydrogenation reaction preferentially activates the methyl C–H bonds first, followed by the activation of the methylene C–H bonds [33]. This indicates that the dehydrogenation reaction on this catalyst follows a stepwise mechanism, where the removal of methyl C–H bond first, followed by the removal of methylene C–H bond.

To understand the reasons for catalyst deactivation, we conducted structural characterization of the catalysts after the reaction. The XRD and N_2 adsorption-desorption results (Fig. S4 and Table S4 in Supporting information) indicate that the framework structure of the catalyst remains unchanged, still exhibiting a typical MFI topology. However, the carbon deposition during the reaction has blocked some pore channels, particularly the mesopores in the catalyst. Given that the structure of the active sites may change during the reaction, we further investigated the structure of the active sites after the reaction (Fig. S5 in Supporting information). The UV–vis results show that the active sites in the 0.5Co/SN-1–0.05 catalyst did not undergo significant changes before and after the reaction, while the signal for the 0.5Co/S-1 sample was less clear due to interference from coke. Subsequently, we analyzed the types of cobalt species in the reacted catalysts using XPS, and the results were consistent with those of the fresh catalysts. This suggests that the deactivation of the catalyst is not caused by changes in the nature of the active sites. The catalysts were subjected to thermogravimetric analysis (TGA) after reacting for 12 h to determine the carbon deposition content. As shown in Fig. 7a, the coke content for 0.5Co/S-1 was 3.84%, whereas for 0.5Co/SN-1–0.05 it was 11.9%. Although the coke content on 0.5Co/SN-1–0.05 was higher than that on 0.5Co/S-1, this is associated with the higher conversion rate of 0.5Co/SN-1–0.05. Under the same conditions, the conversion rate of 0.5Co/SN-1–0.05 was five times that of 0.5Co/S-1. The low conversion rate on 0.5Co/S-1 results in minimal coke deposition, whereas 0.5Co/SN-1–0.05 achieved a high propane conversion rate of 59%, leading to greater coke accumulation over 12 h. Despite the higher coke content, the 0.5Co/SN-1–0.05 catalyst exhibited good performance in stability tests, attributed to the superior coke tolerance of the hierarchical pore structure of the zeolite support. Further characterization of the coke content and types was performed using DTG and Raman spectroscopy. Fig. 7b shows the DTG image of the used samples, showing that the main weight loss peak temperature for 0.5Co/SN-1–0.05 is lower than that of 0.5Co/S-1, indicating that the coke on 0.5Co/SN-1–0.05 is more loosely dispersed and easier to remove by calcination. Fig. 7c shows the UV-Raman spectra of the used samples. The peak at 1581 cm^{-1} corresponds to the C–C stretching vibrations of ordered graphite-like carbon (sp^2 hybridized), while the peak at 1370 cm^{-1} is attributed to the bending vibrations of C–H bonds in disordered carbon (sp^3 hybridized) [33,34]. Ordered car-

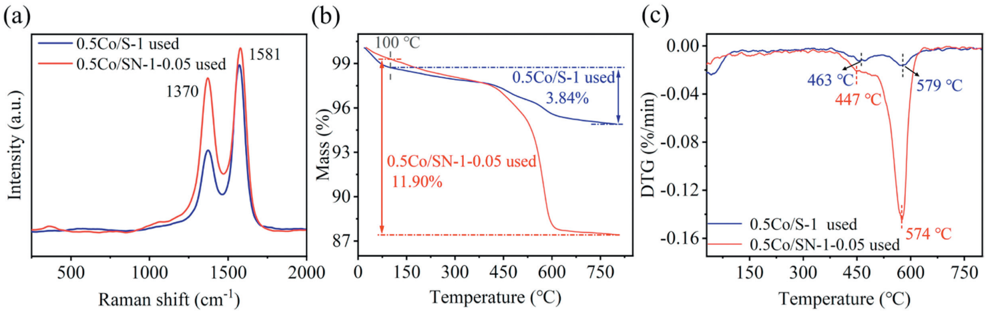

Fig. 7. (a) UV-Raman, (b) TGA and (c) DTG over 0.5Co/S-1 and 0.5Co/SN-1–0.05 catalysts after reaction.

bon is denser and more difficult to remove compared to disordered carbon. The spectra reveal prominent peaks at both 1581cm^{-1} and 1370 cm^{-1}, for both catalysts, with the total peak area for 0.5Co/SN-1–0.05 being significantly larger than that for 0.5Co/S-1, confirming that both catalysts contain coke and that 0.5Co/SN-1–0.05 has more coke. This result is consistent with the TGA data. Additionally, the ratio of the peak areas at 1581 cm^{-1} to 1370 cm^{-1} indicates that 0.5Co/SN-1–0.05 has more loosely dispersed and easily removable disordered carbon, while 0.5Co/S-1 predominantly contains more stable and difficult-to-remove ordered carbon, consistent with the DTG results. The higher coke tolerance and lower weight loss temperature of 0.5Co/SN-1–0.05 contribute to its excellent stability and regeneration performance.

In conclusion, the 0.5Co/SN-1–0.05 catalyst with a meso–microporous structure was successfully prepared using post-treatment with an alkaline solution. The alkaline etching of the zeolite not only introduced mesopores but also generated a substantial number of hydroxyl nests. The resulting mesoporous structure facilitated the easier ingress of $[Co(H_2O)_6]^{2+}$ species into the zeolite pores, while the hydroxyl nests provided abundant anchoring sites for Co species, leading to a more uniform and dispersed distribution. Furthermore, the mesoporous structure demonstrated excellent coke tolerance, mitigating deactivation of the active sites due to coke accumulation. As a result, the 0.5Co/SN-1–0.05 catalyst exhibited significantly superior PDH performance compared to 0.5Co/S-1. Overall, this study provides valuable insights into the synthesis of meso–microporous zeolite catalysts through post-treatment methods.

Declaration of competing interest

The authors declare that they have no known competing financial interests or personal relationships that could have appeared to influence the work reported in this paper.

CRediT authorship contribution statement

Kun Yang: Writing – original draft, Formal analysis, Data curation, Conceptualization. **Anhui Li:** Data curation. **Peng Zhang:** Validation, Investigation. **Guilin Liu:** Software. **Liusai Huang:** Visualization. **Yumeng Fo:** Methodology. **Luyuan Yang:** Investigation. **Xiangyang Ji:** Formal analysis. **Jian Liu:** Supervision, Funding acquisition. **Weiyu Song:** Writing – review & editing, Supervision, Funding acquisition.

Acknowledgments

This work was supported by the National Natural Science Foundation of China (Nos. 22035009, 22178381), the National Key R&D Program of China (Nos. 2021YFA1501301, 2021YFC2901100) and the State Key Laboratory of Heavy Oil Processing (No. 2021–03).

Supplementary materials

Supplementary material associated with this article can be found, in the online version, at doi:10.1016/j.cclet.2024.110663.

References

[1] S. Song, Y. Sun, K. Yang, et al., ACS Catal. 13 (2023) 6044–6067.
[2] Z. Qu, Q. Sun, Inorg. Chem. Front. 9 (2022) 3095–3115.
[3] S. Chen, X. Chang, G. Sun, et al., Chem. Soc. Rev. 50 (2021) 3315–3354.
[4] Z. Qu, T. Zhang, X. Yin, et al., Chem. Res. Chin. Univ. 39 (2023) 870–876.
[5] T. Yang, F. Su, D. Shi, et al., Chin. Chem. Lett. 36 (2025) 110444.
[6] Z. Qu, G. He, T. Zhang, et al., J. Am. Chem. Soc. 146 (2024) 8939–8948.
[7] J. Liu, J. Wang, Y. Zhang, et al., ACS Catal. 13 (2023) 14737–14745.
[8] Z.P. Hu, G. Qin, J. Han, et al., J. Am. Chem. Soc. 144 (2022) 12127–12137.
[9] Z. Huang, D. He, W. Deng, et al., Nat. Commun. 14 (2023) 100.
[10] G. Wang, X. Zhu, C. Li, et al., Chem. Rec. 20 (2020) 604–616.
[11] Z. Lian, C. Si, F. Jan, et al., ACS Catal. 11 (2021) 9279–9292.
[12] M.H. Sun, S.Z. Huang, L.H. Chen, et al., Chem. Soc. Rev. 45 (2016) 3479–3563.
[13] I. Schmidt, A. Boisen, E. Gustavsson, et al., Chem. Mater. 13 (2001) 4416–4418.
[14] J.C. Groen, J.C. Jansen, J.A. Moulijn, et al., J. Phys. Chem. B 108 (2004) 13062–13065.
[15] K. Yang, R. Zhang, H. Xu, et al., Chem. Eng. Sci. 286 (2024) 119651.
[16] C. Chen, M. Sun, C. Weng, et al., Fuel 373 (2024) 132312.
[17] J. Pérez-Ramírez, S. Abelló, A. Bonilla, et al., Adv. Funct. Mater. 19 (2009) 164–172.
[18] T. Wang, Z. Xu, Y. Yue, et al., Chin. J. Chem. Eng. 41 (2022) 384–391.
[19] Y. Chen, X. Zhu, X. Wang, et al., Chem. Eng. J. 419 (2021) 129641.
[20] P.K. Dutta, M. Puri, J. Phys. Chem. A 91 (1987) 4329–4333.
[21] M. Ogura, S. Shinomiya, J. Tateno, et al., Chem. Lett. 29 (2000) 882–883.
[22] S. Abelló, A. Bonilla, J. Pérez-Ramírez, et al., Appl. Catal. A: Gen. 364 (2009) 191–198.
[23] S. Song, K. Yang, P. Zhang, et al., ACS Catal. 12 (2022) 5997–6006.
[24] H. Ronduda, M. Zybert, W. Patkowski, et al., Int. J. Hydrogen Energy 47 (2022) 6666–6678.
[25] B. Hu, W.G. Kim, T.P. Sulmonetti, et al., ChemCatChem 9 (2017) 3330–3337.
[26] S. Lim, D. Ciuparu, C. Pak, et al., J. Phys. Chem. B 107 (2003) 11048–11056.
[27] A. Bellmann, H. Atia, U. Bentrup, et al., Appl. Catal. B: Environ. 230 (2018) 184–193.
[28] S. Li, J. Wang, Y. Ye, et al., Appl. Catal. B: Environ. 263 (2020) 118311.
[29] Y. Yan, Z. Zhang, S.M. Bak, et al., ACS Catal. 9 (2019) 1923–1930.
[30] Y. Dai, Y. Wu, H. Dai, et al., J. Catal. 395 (2021) 105–116.
[31] X. Niu, X. Li, G. Yuan, et al., Ind. Eng. Chem. Res. 59 (2020) 8601–8611.
[32] D. Han, M. Liu, C. Huang, et al., Micropor. Mesopor. Mater. 352 (2023) 112516.
[33] X. Lv, M. Yang, S. Song, et al., ACS Appl. Mater. Interfaces 15 (2023) 14250–14260.
[34] B. Ali, X. Lan, M.T. Arslan, et al., ACS Appl. Nano Mater. 3 (2020) 10966–10977.